

# Color fringe-projected technique for measuring dynamic objects based on bidimensional empirical mode decomposition

Hai-hua Zou, Xiang Zhou,\* Hong Zhao, Tao Yang, Hu-bing Du, Fei-fei Gu, and Zi-xin Zhao

State Key Laboratory Manufacturing Systems Engineering, Xi'an Jiaotong University, Xi'an, Shaanxi 710049, China

\*Corresponding author: zhouxiang@mail.xjtu.edu.cn

Received 5 January 2012; revised 22 April 2012; accepted 23 April 2012;  
posted 23 April 2012 (Doc. ID 160939); published 1 June 2012

A triple-frequency color fringe-projected technique is presented to measure dynamic objects. Three fringe patterns with a carrier frequency ratio of 1:3:9 are encoded in red, green, and blue channels of a color fringe pattern and projected onto an object's surface. Bidimensional empirical mode decomposition is used for decoupling the cross talk among color channels and for extracting the fundamental frequency components of the three fringe patterns. The unwrapped phase distribution of the high-frequency fringe is retrieved by a three-step phase unwrapping strategy to recover the object's height distribution. Owing to its use of only a single snapshot, the technique is suitable for measuring dynamically changing objects with large discontinuity or spatially isolated surfaces. © 2012 Optical Society of America

*OCIS codes:* 120.2830, 120.5050, 120.6650, 330.1710.

## 1. Introduction

With the rapid development in computer technology, three-dimensional (3D) shape measurement, especially for dynamic objects in fast motion, has found wide applications, such as 3D movies and games, web 3D, online quality inspection, human-computer interaction, facial expression capture, and plastic surgery. For real-time 3D shape measurement, the sampled data have to be acquired rapidly, processed quickly, and displayed in a very short period of time. Over the past years, various optical techniques have been developed for real-time 3D shape measurement [1]. Time of flight (TOF) is one of the techniques that has been commercially used [2]. However, accuracy is affected by its fundamental limitations. Stereo vision is another technique widely studied and extensively used [2]. Although this technique could maximize the camera's data acquisition speed, matching the stereo

images is time-consuming and very difficult for uncharacteristic objects.

Fringe projection is a relatively simple technique with the merits of being well established and having fast processing speed. It has found large-scale applications in measuring the 3D shape of dynamic objects. Shape measurement using this technique is carried out by extracting the phase distribution of the fringes. The phase-shifting approach has high accuracy and large measurement range, but the phase-stepping process is time-consuming. By contrast, the Fourier transform approach requires only one fringe pattern, but its measurement range and accuracy are limited by spectrum aliasing [3].

Dynamic measurement may be implemented in a very short time via two methods. One way is to use a single pattern, which can be a composite gray [4–6] or color fringe pattern [7–13]. For the gray pattern-based methods, multifrequency fringes or crossed fringes are composed into a single pattern and projected onto the object's surface. A Fourier transform is often used to separate the components of composite

---

1559-128X/12/163622-09\$15.00/0  
© 2012 Optical Society of America

fringes and retrieve the wrapped phase, which is unwrapped by different phase-unwrapping algorithms. However, this method's measurement range and accuracy are limited by spectrum aliasing. By comparison, color pattern—based techniques could provide more information, but the measurement results are always affected by the variations of the object's surface color and the cross talk among the color channels of commercial CCD and projector. One solution to color decoupling is to add light filters and use a three-chip CCD [7], which inevitably decreases light sensitivity and increases hardware cost. The other solution is calibrating the coefficients with the coupling effects among color channels, which would lead to different results depending on the choice of projector, CCD, and the variation of the object's surface color [7–9,11].

The other way for boosting the speed of measurement is to use multiple patterns while switching them rapidly so that the patterns required for reconstructing the 3D shape can be captured in a short period of time. Huang, Karpinsky, *et al.* proposed a new phase-shifting method using color patterns. Based on the digital projector, the shape acquisition speed can reach 30 frames per second (fps) [14,15]. However, dynamic objects with very high speed may be difficult to measure. In addition, information for phase unwrapping, particularly in measuring large geometries, is insufficient.

This paper proposes a color fringe-projected technique based on bidimensional empirical mode decomposition (BEMD) for the accurate measurement of a dynamic object's shape in a single shot. Three fringe patterns with a carrier frequency ratio of 1:3:9 are encoded in the red, green, and blue channels of a color fringe pattern and projected onto the object's surface by a 3-LCD projector. The deformed color fringe pattern is captured by CCD from another angle. Background trends are eliminated by subtracting the red fringe pattern from both blue and green fringe patterns. BEMD is then employed for decoupling the cross talk among color channels and for separating the high, medium, and low fundamental frequency components, which is followed by phase demodulation. Unwrapped phase distribution of the high-frequency fringe is acquired by a three-step phase-unwrapping strategy. Benefiting from using only a single shot, the proposed technique is able to measure dynamically changing objects with large discontinuity or spatially isolated surfaces.

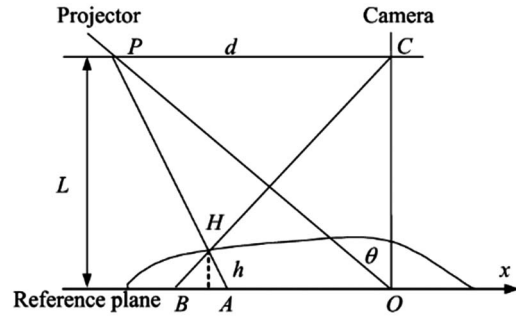


Fig. 1. Optical geometry.

discussed in detail in Section 3. Two experiments, a plaster model and human facial expression, are described in Section 4. Section 5 concludes the paper.

## 2. Principles

### A. Color Fringe-Projected Technique

The classic crossed-optical-axes geometry model for color fringe-projected technique is shown in Fig. 1. The optical axis of the projector lens  $PO$  crosses that of the camera lens  $CO$  at point  $O$  on the reference plane, and the angle between them is  $\theta$ .  $H$  is a point on the object's surface, whereas  $A$  and  $B$  denote two points on the reference plane.  $h(x,y)$  is the height distribution of the object.  $L$  and  $d$  denote the distance between  $C$  and  $O$  and  $C$  and  $P$ , respectively.

Three sinusoidal fringe patterns with 1:3:9 carrier frequency ratio, expressed as Eq. (1), are encoded into the red, green, and blue channels of a color image, respectively, and then projected onto the tested object by a 3-LCD projector.

$$\begin{bmatrix} R(x,y) \\ G(x,y) \\ B(x,y) \end{bmatrix} = \begin{bmatrix} a_r \\ a_g \\ a_b \end{bmatrix} + \begin{bmatrix} b_r \cos(2\pi f_r x) \\ b_g \cos(2\pi f_g x) \\ b_b \cos(2\pi f_b x) \end{bmatrix}, \quad (1)$$

where  $\{a_i, i = r, g, b\}$  represent the background intensities of the red, green, and blue fringe patterns and  $\{b_i, i = r, g, b\}$  represent their amplitudes.  $f_r : f_g : f_b = 1 : 3 : 9$  are the carrier frequencies. A CCD is used to capture the deformed color fringe pattern from another angle. The deformed color fringe pattern with the coupling effect among color channels can be expressed as

$$\begin{bmatrix} g_r(x,y) \\ g_g(x,y) \\ g_b(x,y) \end{bmatrix} = \begin{bmatrix} C_{rr} & C_{rg} & C_{rb} \\ C_{gr} & C_{gg} & C_{gb} \\ C_{br} & C_{bg} & C_{bb} \end{bmatrix} \begin{bmatrix} r_r(x,y) \cdot \{a_r + b_r \cos[2\pi f_r x + \Phi_r(x,y)]\} \\ r_g(x,y) \cdot \{a_g + b_g \cos[2\pi f_g x + \Phi_g(x,y)]\} \\ r_b(x,y) \cdot \{a_b + b_b \cos[2\pi f_b x + \Phi_b(x,y)]\} \end{bmatrix} + \begin{bmatrix} n_r(x,y) \\ n_g(x,y) \\ n_b(x,y) \end{bmatrix}, \quad (2)$$

The paper is organized as follows. Section 2 gives the basic principles of the color fringe-projected technique based on BEMD. The simulation results are

where  $\{C_{ij} \leq 1, i, j = r, g, b\}$  are the coefficients representing the coupling effects among color channels and  $C_{ij} = 1$  if  $i = j$ .  $\{r_i(x,y), i = r, g, b\}$  are the

reflectivity distributions.  $\{n_i(x, y), i = r, g, b\}$  indicate the noise.  $\{\Phi_i(x, y), i = r, g, b\}$  represent the phase modulation caused by height distribution  $h(x, y)$ . We denote  $A_i(x, y) = r_i(x, y)a_i$ ,  $B_i(x, y) = r_i(x, y)b_i$ , and  $(i = r, g, b)$ , and Eq. (2) then is replaced with

$$\begin{bmatrix} g_r(x, y) \\ g_g(x, y) \\ g_b(x, y) \end{bmatrix} = \begin{bmatrix} C_{rr} & C_{rg} & C_{rb} \\ C_{gr} & C_{gg} & C_{gb} \\ C_{br} & C_{bg} & C_{bb} \end{bmatrix} \begin{bmatrix} A_r(x, y) + B_r \cos[2\pi f_r x + \Phi_r(x, y)] \\ A_g(x, y) + B_g \cos[2\pi f_g x + \Phi_g(x, y)] \\ A_b(x, y) + B_b \cos[2\pi f_b x + \Phi_b(x, y)] \end{bmatrix} + \begin{bmatrix} n_r(x, y) \\ n_g(x, y) \\ n_b(x, y) \end{bmatrix}. \quad (3)$$

When  $L \gg h(x, y)$ ,

$$\begin{aligned} h(x, y) &= -\frac{L\Delta\Phi_i(x, y)}{2\pi f_i d} \\ &= -\frac{L}{2\pi f_i d} [\Phi_i(x, y) - \Phi_{0i}(x, y)], \\ &(i = r, g, b), \end{aligned} \quad (4)$$

where  $\{\Phi_{0i}(x, y), i = r, g, b\}$  are the phase values of the fringe pattern on reference plane. Our goal is to obtain the unwrapped phase  $\Delta\Phi_b(x, y)$  [ $\Delta\Phi_b(x, y) = \Phi_b(x, y) - \Phi_{0b}(x, y)$ ] of the high-frequency fringe, from which the height distribution of the object is recovered. To achieve this goal, two problems have to be solved. One is decoupling the cross talk, which impedes the extraction of the fundamental frequency components, and the other is phase unwrapping. To solve these problems, a BEMD-based algorithm and a three-step phase unwrapping strategy are presented in the next two sections, respectively.

## B. Color Decoupling and Fundamental Frequency Components Extraction

The empirical mode decomposition (EMD) proposed by Huang *et al.* [16] is a data-driven signal-processing algorithm that could analyze nonlinear and nonstationary data by obtaining local features and time-frequency distribution of the data. EMD and its variants have also been used to analyze fringe patterns for denoising, detrending, and phase retrieval in recent years. The standard EMD was used to reduce noise and normalize fringes in a digital speckle pattern [17]. Li *et al.* used one-dimensional (1D) EMD to eliminate the zero spectrum in Fourier transform profilometry [18]. We used multi-variate EMD [19] and ensemble EMD [20] for noise reduction and phase extraction of carrier fringe patterns.

In 1D EMD methods, each row or column in the fringe patterns is processed sequentially, which ignores the correlation among the rows or columns of a two-dimensional (2D) image and thus probably leads to undesirable results for heavily warped fringes. Moreover, 1D EMD is sensitive to noise and possibly fails to decompose the fringe patterns with noise. To overcome these problems, BEMD has been applied to analyze speckle patterns [21] and amplitude-encoded fringe patterns [22]. BEMD employs local 2D extrema and surface interpolation

to estimate local envelopes, making it suitable for analyzing fringe patterns with large deformation. Hence, we choose BEMD to extract the fundamental frequency components and decouple the cross talk among color channels of the images.

### 1. Steps for BEMD

If we denote the original image as  $I$ , the bidimensional intrinsic mode function (BIMF) as  $F$ , and the residue as  $R$ , then the sifting process of BEMD is summarized as follows:

- (1) Identify the extrema (both maxima and minima) maps of  $I$ .
- (2) Estimate the upper and lower envelopes from the maxima and minima points, respectively.
- (3) Determine the local mean  $m_1$  by averaging the two envelopes.
- (4) Subtract the mean from  $I$ :  $h_1 = I - m_1$ .
- (5) Repeat steps (1) to (4) as  $h_1$  is a BIMF, and set  $F = h_1$ .
- (6) The residue is calculated:  $R = I - F$ .

Let  $R$  be a new original image and repeat the above steps; then  $I$  can be de separated into a series of BIMFs.

The implementation of BEMD strongly depends on the algorithms of extrema detection and envelope estimation. Nunes *et al.* proposed a new BEMD algorithm that uses morphological reconstruction and radial basis function (RBF) for extrema detection and surface interpolation, respectively [23,24]. The new BEMD algorithm performed well in image and texture analysis, and is therefore adopted in our method.

#### A. Extrema Detection Using Morphological Reconstruction [23]

The extrema are detected by morphological reconstruction based on geodesic operators. For identifying the maxima maps, we take  $J = I - 1$  and perform the reconstruction  $I_{\text{rec}}$  (by geodesic dilation) of  $J$  by  $I$ . The difference  $I - I_{\text{rec}}$  corresponds to the indicator function of the maxima of  $I$ . Conversely, the difference between  $I_{\text{rec}}^*$  (reconstruction by geodesic erosion) and  $I$  produces the indicator function of the minima of  $I$ . This extrema detection method is described in detail in [25]. Compared with the neighboring window method, this technique is faster and more precise.

#### B. Surface Interpolation by RBF [23,26]

RBF-based interpolation methods impose fewer restrictions on the geometry of the interpolation centers and are suited to problems where the interpolation centers do not form a regular grid. In addition, they are some of the most elegant schemes from a

mathematical point of view and do not create distortions near the end points, and they show superior performance in scattered data interpolation. The RBF function form is given as follows:

$$s(x) = p_m(x) + \sum_{i=1}^N \lambda_i \Phi(\|x - x_i\|), \quad x \in R^d, \lambda_i \in R, \quad (5)$$

where

- $s$  is the radial basis function;
- $p_m$  is a low-degree polynomial, typically linear or quadratic, a member of the  $m$ th-degree polynomials in  $d$  variables;
- $\|\cdot\|$  denotes the Euclidean norm;
- the  $\lambda_i$ 's are the RBF coefficients;
- $\Phi$  is a real-valued function called the basis function; and
- $x_i$ 's are the RBF centers.

Many choices of  $\Phi$  are available for various RBFs [26]. RBF-thin-plate spline, one of the classical forms, is adopted in this paper. The form of  $\Phi$  for RBF-thin-plate spline is as follows:

$$\Phi(r) = r^2 \log(r). \quad (6)$$

## 2. Extraction of Fundamental Frequency Components Based on BEMD

The cross talk and background trends impede the extraction of the fundamental frequency components. In our method, the background trends are eliminated by subtracting the red fringe pattern from that of both blue and green. Then an approach for extraction of fundamental frequency components based on BEMD is used for color decoupling, which is described as follows:

(1) Eliminate the background trends by subtracting the red fringe pattern from that of both blue and green. Supposing the background trends of the red, green, and blue fringe patterns are approximately the same, as shown in Eq. (7), the background trends would be eliminated substantially, giving the result as Eq. (8). The residual background trends have little effect on the following processes.

(2) Denoise using the 2D discrete wavelet transform (2D DWT). Notably, the high fundamental frequency component in  $f_{\text{Mid},\text{low}}(x,y)$  should be filtered in order to obtain better results without mode mixing.

(3) Decompose  $f_{\text{Mid},\text{low}}(x,y)$  using the BEMD algorithm in Subsection 2.A.1. The resulting BIMF1 and BIMF2 correspond to the fundamental frequency components of the medium- and low-frequency fringe, denoted as  $\bar{g}_g(x,y)$  and  $\bar{g}_r(x,y)$ , respectively.

(4) Apply the above step to  $f_{\text{High},\text{low}}(x,y)$  and BIMF1 indicates the high fundamental frequency component, denoted as  $\bar{g}_b(x,y)$ .

$$\begin{bmatrix} \bar{g}_r(x,y) \\ \bar{g}_g(x,y) \\ \bar{g}_b(x,y) \end{bmatrix} = \begin{bmatrix} (C_{gr} - C_{rr})B_r(x,y) \cdot \cos[2\pi f_r x + \Phi_r(x,y)] \\ (C_{gg} - C_{rg})B_g(x,y) \cdot \cos[2\pi f_g x + \Phi_g(x,y)] \\ (C_{bb} - C_{rb})B_b(x,y) \cdot \cos[2\pi f_b x + \Phi_b(x,y)] \end{bmatrix}. \quad (9)$$

The background trends are greatly depressed by subtracting the red fringe pattern from that of both blue and green, and color cross talk is decoupled by BEMD; only the fundamental frequency components remain as the major part of each fringe pattern. Hence, phase distribution  $\{\Phi_i(x,y), i = r, g, b\}$  of the three fringe patterns can be easily demodulated via 2D Fourier transform without spectrum aliasing.

Similarly, the phase value of the fringe pattern on reference plane  $\{\Phi_{0i}(x,y), i = r, g, b\}$  can be extracted by the same strategy.

### C. Three-Step Phase Unwrapping

The phase  $(\Delta\varphi_i(x,y), i = r, g, b)$  demodulated via 2D Fourier transform is wrapped from  $-\pi$  to  $\pi$  and must be unwrapped. A three-step phase-unwrapping strategy is developed, according to the temporal phase-unwrapping strategy proposed by Zhao *et al.* [27]. The phase distribution of the low-frequency fringe with the least wraps or even no wrap is used to unwrap that of the medium-frequency fringe, then the medium unwraps the high. Finally, the unwrapped phase distribution of the high-frequency fringe is retrieved to recover the height distribution of the object. The wrapped phase is unwrapped point

$$\begin{bmatrix} C_{rr} \\ C_{rg} \\ C_{rb} \end{bmatrix}^T \begin{bmatrix} A_r(x,y) \\ A_g(x,y) \\ A_b(x,y) \end{bmatrix} \approx \begin{bmatrix} C_{gr} \\ C_{gg} \\ C_{gb} \end{bmatrix}^T \begin{bmatrix} A_r(x,y) \\ A_g(x,y) \\ A_b(x,y) \end{bmatrix} \approx \begin{bmatrix} C_{br} \\ C_{bg} \\ C_{bb} \end{bmatrix}^T \begin{bmatrix} A_r(x,y) \\ A_g(x,y) \\ A_b(x,y) \end{bmatrix}. \quad (7)$$

$$\begin{bmatrix} f_{\text{Mid},\text{low}}(x,y) \\ f_{\text{High},\text{low}}(x,y) \end{bmatrix} = \begin{bmatrix} g_g(x,y) - g_r(x,y) \\ g_b(x,y) - g_r(x,y) \end{bmatrix} \approx \begin{bmatrix} C_{gr} - C_{rr} & C_{gg} - C_{rg} & C_{gb} - C_{rb} \\ C_{br} - C_{rr} & C_{bg} - C_{rg} & C_{bb} - C_{rb} \end{bmatrix} \times \begin{bmatrix} B_r(x,y) \cdot \cos[2\pi f_r x + \Phi_r(x,y)] \\ B_g(x,y) \cdot \cos[2\pi f_g x + \Phi_g(x,y)] \\ B_b(x,y) \cdot \cos[2\pi f_b x + \Phi_b(x,y)] \end{bmatrix} + \begin{bmatrix} n_g(x,y) - n_r(x,y) \\ n_b(x,y) - n_r(x,y) \end{bmatrix}. \quad (8)$$

by point, from one phase map to another, without the help of the neighboring points' phase. Therefore, the process is very fast and reliable. Suppose the unwrapped phase values are denoted as  $\Delta\Phi_i(x,y)$ ,  $i = r, g, b$  and given by

$$\Delta\Phi_r(x,y) = \Delta\varphi_r(x,y), \quad (10)$$

$$\Delta\Phi_i(x,y) = \Delta\varphi_i(x,y) + 2n_i(x,y)\pi, \quad (i=g,b). \quad (11)$$

The three-step phase-unwrapping strategy is described in detail as follows:

(1) The phase distribution of the low-frequency fringe with the least wraps or even no wrap is used to unwrap that of the medium-frequency fringe.

$$\begin{aligned} n_G(x,y) &= \text{INT} \left[ \frac{\Delta\Phi_g(x,y)}{2\pi} \right] \\ &= \text{INT} \left[ \frac{k_r \Delta\Phi_r(x,y) / k_g - \Delta\varphi_g(x,y)}{2\pi} \right], \end{aligned} \quad (12)$$

where INT is an operator equal to the integer part of its argument, and  $k_r, k_g$  are isolated constants determined by Eq. (4):  $k_r = -\frac{L}{2\pi f_r d}$ ,  $k_g = -\frac{L}{2\pi f_g d}$ .

(2) Considering the influence of noise and calibration errors, the result obtained by Eq. (12) should be revised. Define the difference between the height distributions obtained from the medium- and low-frequency fringes as the quantity

$$\begin{aligned} \Delta(m) &= k_g[\Delta\varphi_g(x,y) + 2m\pi] - k_r \Delta\Phi_r(x,y), \\ [m &= n_G(x,y), n_G(x,y) \pm 1], \end{aligned} \quad (13)$$

where  $m$  is termed  $m_{0g}(x,y)$  when  $\Delta(m)$  reaches its minimum. Finally, the unwrapped distribution  $\Delta\Phi_g(x,y)$  is

$$\Delta\Phi_g(x,y) = \Delta\varphi_g(x,y) + 2m_{0g}(x,y)\pi. \quad (14)$$

(3) Subsequently, the unwrapped phase distribution of the medium-frequency fringe  $\Delta\Phi_g(x,y)$  is used to unwrap  $\Delta\varphi_b(x,y)$ , resulting in  $\Delta\Phi_b(x,y)$ .

### 3. Computer Simulation

Based on Eq. (2), a  $512 \times 512$  pixel image of a deformed color fringe pattern contaminated by Gaussian white noise with constant mean and variance is generated by the computer software and is shown in Fig. 2. The color coupling effects of commercial CCDs and projectors vary from one combination to another, but the coefficients are normally between 0.1 and 0.4 according to our experience and [9]. For simplicity, the uniform coefficient value is simulated, ignoring the minor difference among channels. Specifically, the coupling coefficients  $C_{ij}$  are set to 0.2 if  $i \neq j$ , and to 1 if  $i = j$ ; that is,  $\{C_{ij} = 0.2, i \neq j; C_{ij} = 1, i = j\}$ . The background intensities  $a_i$ ,

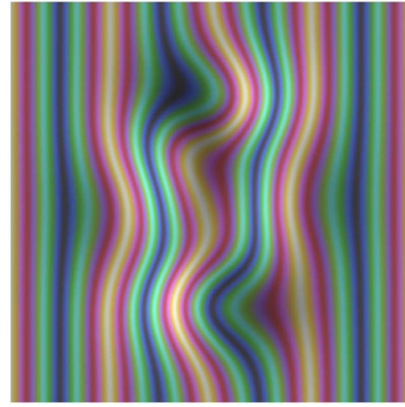


Fig. 2. (Color online) Deformed color fringe pattern.

( $i = r, g, b$ ) and their amplitudes  $b_i$ , ( $i = r, g, b$ ) are set to 40 and 18, respectively, so that the maxima of the deformed fringe pattern are 37 while the minima are 248. Other parameters are set as follows:

- Normalized carrier frequencies:  $f_r = 1/128$ ,  $f_g = 3f_r$ ,  $f_b = 9f_r$ .
- Phase distribution:

$$\begin{aligned} \Phi_r(x,y) &= P(x,y), \\ \Phi_g(x,y) &= 3P(x,y), \\ \Phi_b(x,y) &= 9P(x,y), \end{aligned} \quad (15)$$

where

$$\begin{aligned} P(x,y) &= 3 \left[ 3(1-x)^2 e^{-x^2-(y+1)^2} \right. \\ &\quad \left. - 10 \left( \frac{x}{5} - x^3 - y^5 \right) e^{-x^2-y^2} - \frac{1}{3} e^{-(x+1)^2-y^2} \right] / 8, \\ (x,y) &= 1, 2 \dots 512, \end{aligned} \quad (16)$$

and it can be generated by the peaks function provided by the MATLAB function base.

- The reflectivity distribution:  $\{r_i(x,y) = 3 + 40\Phi_i(x,y), i = r, g, b\}$ .

The true fundamental frequency components of the deformed color fringe pattern are shown in Figs. 3(a) through 3(c), whereas those extracted by the color decoupling algorithm based on BEMD are shown in Figs. 3(d) through 3(f). The low, medium, and high fundamental frequency components are extracted accurately without mode mixing. Then the wrapped phase distribution of the three fringe patterns, (as shown in Figs. 4(a) through 4(c), is demodulated via 2D Fourier transform, followed by phase unwrapping using the three-step phase unwrapping strategy. Figures 4(d) and 4(e) show the unwrapped phase maps of the medium- and high-frequency fringes, respectively, and Fig. 4(f) is the absolute error map. The maximum of the absolute error map is 0.3408, only 0.69% of the peak value. This result shows that the method can achieve high precision.

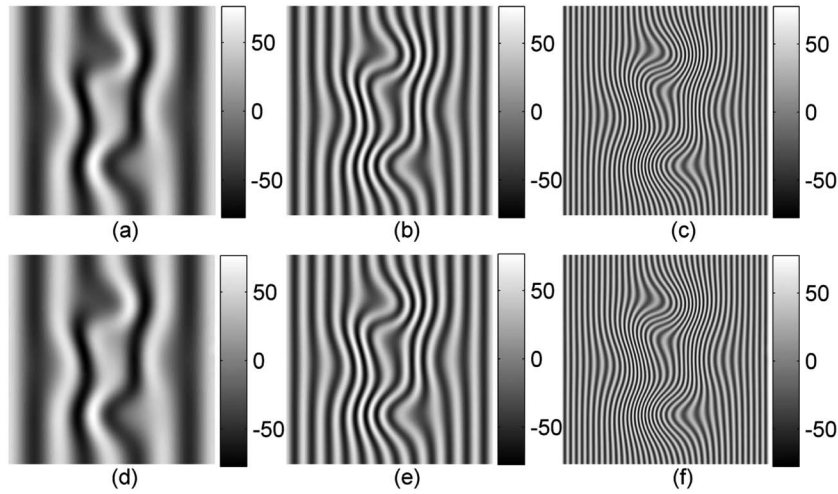


Fig. 3. True (a) low; (b) medium; and (c) high fundamental frequency components; and (d) low; (e) medium and (f) high ones extracted by color decoupling algorithm based on BEMD.

#### 4. Experiments

The experimental setup in Fig. 5(a) is applied in our experiments. We use a Sony VPL-EX175 3-LCD projector for the fringe projection. The projector has the brightness of 3600 ANSI lumens, a contrast ratio of 2500:1, and a standard resolution of  $1024 \times 768$  (XGA). An 8 bit CCD camera (AVT Guppy F-146C) is used for image capture. This camera uses a color CCD sensor (Sony ICX267) that produces color images based on the Bayer color filter array technique. It runs at up to 17.7 fps at full resolution ( $1392 \times 1040$ ). However, the overlapping spectra between the neighboring channels causes heavy color coupling, and the discrepant behavior of each channel causes imbalance of the three color channels. The image card used in the experiments is MV-1394A, the transmission of which is 400 Mbits/s.

##### A. Calibration of Gray-Scale Curve

In the fringe-projected techniques for 3D shape measurement, a linear gray-scale curve, which

represents the relationship between the input and output gray-scale value, is desired for higher measurement accuracy. However, the intensity response between commercial projectors and CCDs is non-linear, and the accuracy is affected by color imbalance caused by the mismatch of the color spectra of the projector and camera, so calibration of the gray-scale curve is necessary. We use the method proposed in [14] to calibrate the gray-scale curve for the red, green, and blue channels in our experiments. After calibrating the gray-scale curve, the linearity of the fringe is much better and the background trends of the red, green, and blue fringe patterns are approximately the same.

##### B. Contrast Experiment

A plaster model of a human face, as shown in Fig. 5(b), is used as the tested object. A triple-frequency color fringe pattern with 1:3:9 carrier frequency ratio (the pixel periods of the red, green, and blue channel fringes are 81, 27, and 9 pixels, whereas

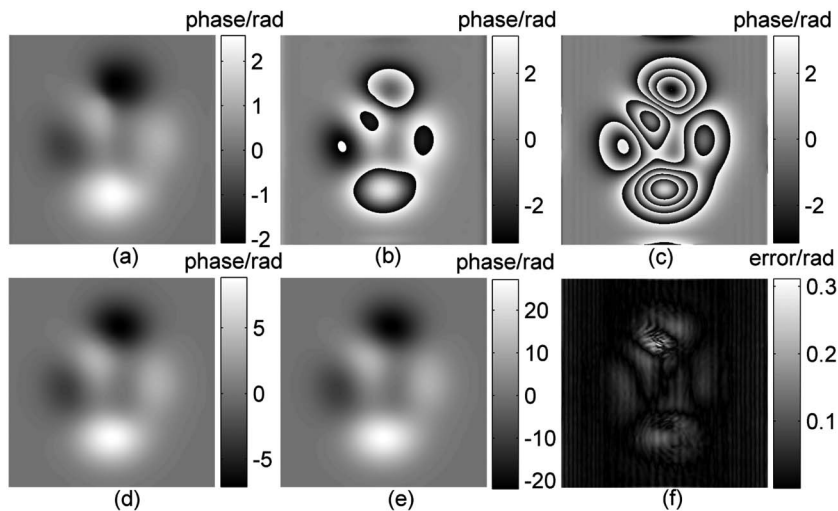


Fig. 4. Wrapped phase distribution of (a) low- (no phase wrap); (b) medium-; and (c) high-frequency fringes; unwrapped phase maps of (d) medium- and (e) high-frequency fringes; and (f) absolute error map.

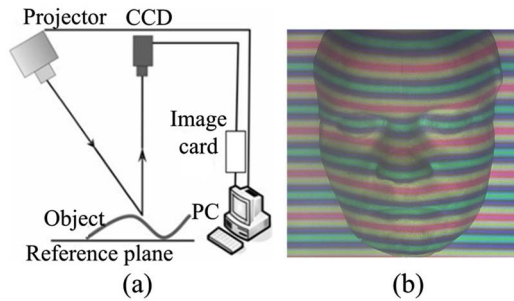


Fig. 5. (Color online) (a) Experimental setup and (b) deformed color fringe pattern.

the real periods are 45, 15, and 5 mm, respectively) is projected onto the tested object by a 3-LCD projector. The deformed fringe pattern captured by CCD is analyzed using the proposed method.

Then the image is sent to the computer and separated into red, green, and blue fringe patterns as

shown in Figs. 6(a) through 6(c). The color decoupling algorithm based on BEMD is used to extract the fundamental frequency components, and the accurate results are shown in Figs. 6(d) through 6(f). Accordingly, three wrapped phase maps are demodulated via 2D Fourier transform and shown in Figs. 7(a) through 7(c). Using the three-step phase unwrapping strategy, the unwrapped phase distribution of the low-, medium-, and high-frequency fringes as shown in Figs. 7(d) through 7(f) are acquired.

A four-step-phase-shifting method is used for comparison to prove the feasibility of the proposed technique. The 3D reconstruction of the restored phase distribution obtained by the two methods is shown in Fig. 8. Figures 8(a) and 8(b) show the restored phase distribution by the four-step-shifting and proposed methods, respectively, whereas Fig. 8(c) shows the results of the 256th column. The results reveal that the unwrapped phase is successfully retrieved

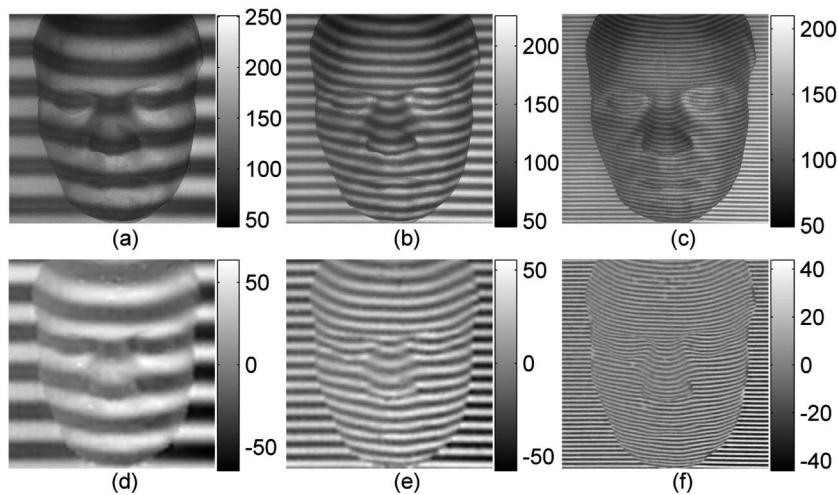


Fig. 6. (a) Red; (b) green; and (c) blue fringe patterns from the captured image; and (d) low; (e) medium; and (f) high fundamental frequency components extracted by color decoupling algorithm based on BEMD.

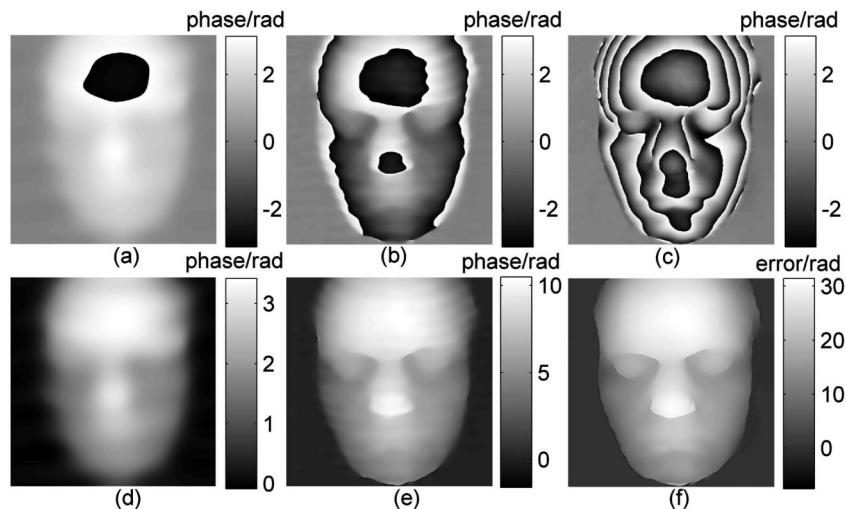


Fig. 7. Wrapped phase maps of (a) low- (with little phase wraps); (b) medium-; and (c) high-frequency fringes, and unwrapped phase maps of (d) low-; (e) medium-; and (f) high-frequency fringes.

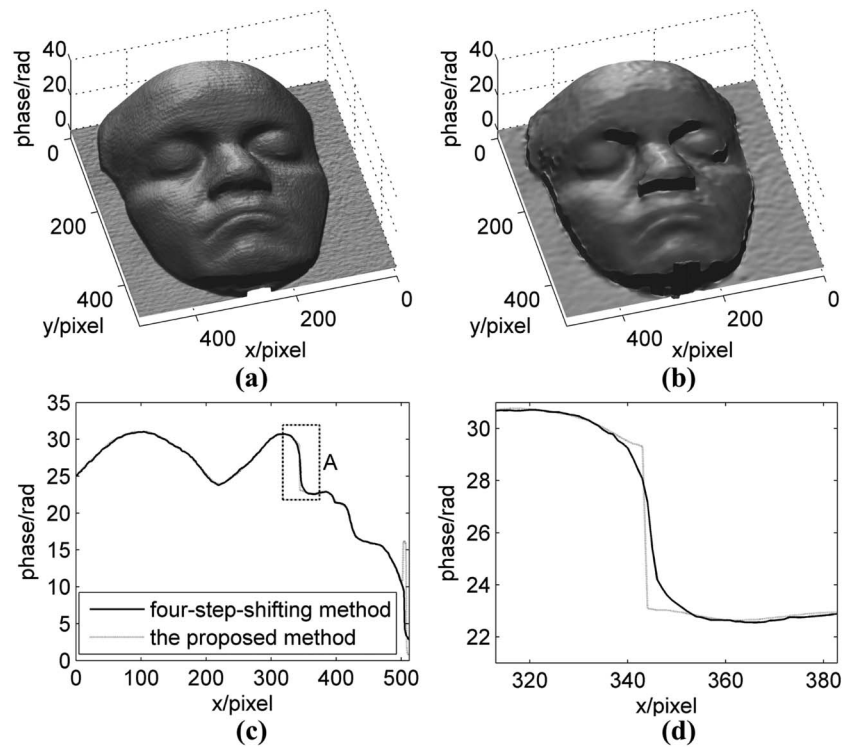


Fig. 8. Restored phase distribution by (a) four-step-shifting method and (b) the proposed method; (c) the results of the 256th column by the two methods; and (d) a detailed view of A in (c).

by the proposed method. However, in the areas close to the borders, the results are not perfect because the results of envelope estimation using RBF interpolation are different from the actual fringe curve, in which the height is dramatically changed. Figure 8(d) shows a detailed view of A with abrupt height, which is one part of 8(c).

### C. Experiment on Facial Expression Capture

The technique is also used for facial expression capture. Under the same circumstances as in the contrast experiment, 66 frames of color deformed fringe patterns are continuously captured by CCD camera. Figures 9(a) through 9(c) show only three frames of

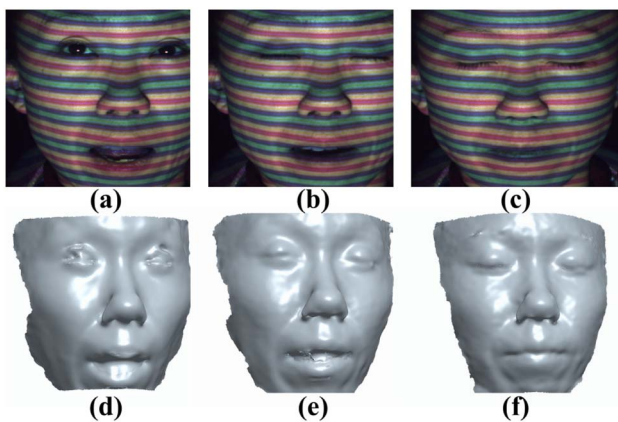


Fig. 9. (Color online) (a) Surprised, (b) sad, and (c) chuckle expressions; 3D reconstruction results of (d) surprised, (e) sad, and (f) chuckle expressions.

them (namely surprised, sad, and chuckle expressions). The 3D reconstruction results of the restored phase distribution of high-frequency fringes are shown in Figs. 9(d) through 9(f). The unwrapped phase is successfully restored, except for some areas close to the borders and other areas with abrupt texture, such as the teeth, eyes and tongue. These results are caused by the inherent defect of fringe-projected techniques, which are not qualified for measuring objects with abrupt texture.

### 5. Conclusion

The paper proposed a color fringe-projected technique with the potential for full-field dynamic 3D shape measurement. By subtracting the red fringe pattern from that of both blue and green, the background trends are greatly eliminated. The color cross talk problem is solved by a color decoupling algorithm based on BEMD. Using a three-step phase unwrapping strategy, the unwrapped phase distribution of the high-frequency fringe is recursively acquired to recover the object's height distribution. In this technique, only a commercial off-the-shelf projector and CCD are needed, so the hardware cost is greatly decreased compared with the previous techniques using light filters and three-chip CCDs. This technique can be implemented for 3D shapes measurement of objects with large discontinuity or spatially isolated surfaces. Because only a single snapshot is required, the technique allows the instantaneous measurement of 3D shapes for fast-moving, dynamic objects.

This research was supported by the National Natural Science Foundation (Grant No. 51105301) and the National Basic Research Program (Grant No. 2011CB706805) of China. We also acknowledge the support from the Scientific Research Program of Xi'an City (CX1007) and the Innovation Fund for Undergraduate Research Training and Practice, Xi'an Jiaotong University.

## References

1. E. Stoykova, A. A. Alatan, P. Benzie, N. Grammalidis, S. Malassiotis, J. Ostermann, S. Piekh, V. Sainov, C. Theobalt, T. Thevar, and X. Zabulis, "3-D time-varying scene capture technologies—a survey," *IEEE Trans. Circ. Syst. Video Technol.* **17**, 1568–1586 (2007).
2. S. Zhang, "Recent progresses on real-time 3D shape measurement using digital fringe projection techniques," *Opt. Lasers Eng.* **48**, 149–158 (2010).
3. M. Takeda and K. Mutoh, "Fourier transform profilometry for the automatic measurement of 3-D object shapes," *Appl. Opt.* **22**, 3977–3982 (1983).
4. W.-H. Su and H. Liu, "Calibration-based two-frequency projected fringe profilometry: a robust, accurate, and single-shot measurement for objects with large depth discontinuities," *Opt. Express* **14**, 9178–9187 (2006).
5. M. Takeda, Q. Gu, M. Kinoshita, H. Takai, and Y. Takahashi, "Frequency-multiplex Fourier-transform profilometry: a single-shot three-dimensional shape measurement of objects with large height discontinuities and/or surface isolations," *Appl. Opt.* **36**, 5347–5354 (1997).
6. H.-M. Yue, X.-Y. Su, and Y.-Z. Liu, "Fourier transform profilometry based on composite structured light pattern," *Opt. Laser Technol.* **39**, 1170–1175 (2007).
7. J. Pan, P. S. Huang, and F.-P. Chiang, "Color phase-shifting technique for three-dimensional shape measurement," *Opt. Eng.* **45**, 013602 (2006).
8. L. Kinell, "Multichannel method for absolute shape measurement using projected fringes," *Opt. Lasers Eng.* **41**, 57–71 (2004).
9. P. S. Huang, Q. Hu, F. Jin, and F.-P. Chiang, "Color-encoded digital fringe projection technique for high-speed three-dimensional surface contouring," *Opt. Eng.* **38**, 1065–1071 (1999).
10. Z. Zhang, D. P. Towers, and C. E. Towers, "Snapshot color fringe projection for absolute three-dimensional metrology of video sequences," *Appl. Opt.* **49**, 5947–5953 (2010).
11. Z. Zhang, C. E. Towers, and D. P. Towers, "Time efficient color fringe projection system for 3D shape and color using optimum 3-frequency selection," *Opt. Express* **14**, 6444–6455 (2006).
12. W.-H. Su, "Projected fringe profilometry using the area-encoded algorithm for spatially isolated and dynamic objects," *Opt. Express* **16**, 2590–2596 (2008).
13. W.-H. Su, "Color-encoded fringe projection for 3D shape measurements," *Opt. Express* **15**, 13167–13181 (2007).
14. P. S. Huang, C. Zhang, and F.-P. Chiang, "High-speed 3-D shape measurement based on digital fringe projection," *Opt. Eng.* **42**, 163–168 (2003).
15. N. Karpinsky, S. Lei, and S. Zhang, "High-resolution, real-time fringe pattern profilometry," *Proc. SPIE* **7522**, 75220E (2009).
16. N. E. Huang, Z. Shen, S. R. Long, M. C. Wu, H. H. Shih, Q. Zheng, N.-C. Yen, C. C. Tung, and H. H. Liu, "The empirical mode decomposition and the Hilbert spectrum for nonlinear and non-stationary time series analysis," *Proc. Roy. Soc. Lond. Math. Phys. Sci.* **454**, 903–995 (1998).
17. M. B. Bernini, G. E. Galizzi, A. Federico, and G. H. Kaufmann, "Evaluation of the 1D empirical mode decomposition method to smooth digital speckle pattern interferometry fringes," *Opt. Lasers Eng.* **45**, 723–729 (2007).
18. S. Li, X. Su, W. Chen, and L. Xiang, "Eliminating the zero spectrum in Fourier transform profilometry using empirical mode decomposition," *J. Opt. Soc. Am. A* **26**, 1195–1201 (2009).
19. X. Zhou, T. Yang, H. H. Zou, and H. Zhao, "A multivariate empirical mode decomposition approach for adaptive denoising of fringe patterns," *Opt. Lett.* **37**, 1904–1906 (2012).
20. X. Zhou, H. Zhao, and T. Jiang, "Adaptive analysis of optical fringe patterns using ensemble empirical mode decomposition algorithm," *Opt. Lett.* **34**, 2033–2035 (2009).
21. M. B. Bernini, A. Federico, and G. H. Kaufmann, "Noise reduction in digital speckle pattern interferometry using bidimensional empirical mode decomposition," *Appl. Opt.* **47**, 2592–2598 (2008).
22. M. Wielgus and K. Patorski, "Evaluation of amplitude encoded fringe patterns using the bidimensional empirical mode decomposition and the 2D Hilbert transform generalizations," *Appl. Opt.* **50**, 5513–5523 (2011).
23. J. C. Nunes, Y. Bouaoune, E. Delechelle, O. Niang, and P. Bunel, "Image analysis by bidimensional empirical mode decomposition," *Image Vis. Comput.* **21**, 1019–1026 (2003).
24. J. C. Nunes, S. Guyot, and E. Deléchelle, "Texture analysis based on local analysis of the bidimensional empirical mode decomposition," *Mach. Vis. Appl.* **16**, 177–188 (2005).
25. L. Vincent, "Morphological grayscale reconstruction in image analysis: applications and efficient algorithms," *IEEE Trans. Image Process.* **2**, 176–201 (1993).
26. S. M. A. Bhuiyan, N. O. Attoh-okine, K. E. Barner, A. Y. Ayenu-prah, and R. R. Adhami, "Bidimensional empirical mode decomposition using various interpolation techniques," *Adv. Adapt. Data. Anal.* **1**, 309–338 (2009).
27. H. Zhao, W. Chen, and Y. Tan, "Phase-unwrapping algorithm for the measurement of three-dimensional object shapes," *Appl. Opt.* **33**, 4497–4500 (1994).